

See discussions, stats, and author profiles for this publication at: <https://www.researchgate.net/publication/229058476>

Multinuclear solid-state NMR studies of ordered mesoporous bioactive glasses

ARTICLE *in* THE JOURNAL OF PHYSICAL CHEMISTRY C · JUNE 2008

Impact Factor: 4.77

CITATIONS

14

READS

16

7 AUTHORS, INCLUDING:



Isabel Izquierdo-Barba

Complutense University of Madrid

86 PUBLICATIONS 3,149 CITATIONS

SEE PROFILE



Daniel Arcos

Complutense University of Madrid

89 PUBLICATIONS 3,584 CITATIONS

SEE PROFILE



Mattias Edén

Stockholm University

109 PUBLICATIONS 3,017 CITATIONS

SEE PROFILE

Multinuclear Solid-State NMR Studies of Ordered Mesoporous Bioactive Glasses

Ekaterina Leonova,[†] Isabel Izquierdo-Barba,[‡] Daniel Arcos,[‡] Adolfo López-Noriega,[‡] Niklas Hedin,[§] Maria Vallet-Regí,[‡] and Mattias Edén^{*,†}

Physical Chemistry Division, Arrhenius Laboratory, Stockholm University, SE-106 91, Stockholm, Sweden, Departamento de Química Inorgánica y Bioinorgánica, Facultad de Farmacia, Universidad Complutense de Madrid, 28040-Madrid, Spain, Centro de Investigación Biomédica en Red. Bioingeniería, Biomateriales y Nanomedicina, CIBER-BBN, Spain, and Inorganic Chemistry Division, Arrhenius Laboratory, Stockholm University, SE-106 91, Stockholm, Sweden

Received: November 12, 2007; In Final Form: January 22, 2008

The local structures of highly ordered mesoporous bioactive CaO–SiO₂–P₂O₅ glasses were investigated for variable Ca contents. ¹H NMR revealed a diversity of hydrogen-bonded and “isolated” surface silanols as well as adsorbed water molecules. The structural roles of Si and P were explored using a combination of ²⁹Si and ³¹P magic-angle spinning (MAS) nuclear magnetic resonance (NMR) techniques; the proximities of Si and P to protons were studied through cross-polarization-based experiments, including ¹H–²⁹Si and ¹H–³¹P hetero-nuclear two-dimensional correlation spectroscopy. The results are consistent with SiO₂ being the main pore-wall component, whereas P is present as a separate amorphous calcium orthophosphate phase, which is dispersed over the pore wall as nanometer-sized clusters. The excess Ca that is not consumed in the phosphate phase modifies the silica glass network where it associates at/near the mesoporous surface. This biphasic structural model of the pore wall leads to the high accessibility of both Ca and P to body fluids, and its relation to the experimentally demonstrated high in vitro bioactivities of these materials is discussed.

1. Introduction

Bioactive glasses (BGs) have since their discovery¹ more than three decades ago been subject to intensive research and developments,^{2,3} stemming from their bone-bonding ability. This “bioactive” feature derives from the formation of a biomimicking calcium-deficient hydroxycarbonate apatite (HCA) surface layer of the glass on its contact with body fluids. The HCA layer has a similar composition as the inorganic constituents of bones and teeth. Here, the degree of bioactivity of a glass specimen refers to its formation rate of HCA on body fluid exposure; in practice, this is assessed in vitro using a simulated body fluid (SBF).^{2,3} The BG surface layer is believed to constitute initially an amorphous calcium phosphate phase, which subsequently crystallizes into HCA. However, the presence of amorphous phosphate phases during bone formation is still debated.⁴

BGs were initially prepared by a traditional quenching of melts of the (Na₂O)–CaO–SiO₂–P₂O₅ system.^{1–3} However, the introduction of the sol–gel technique allowed the preparation of SiO₂-richer compositions, leading to more homogeneous BGs that displayed higher bioactivities.^{3,5–12} The bioactivity of both melt- and gel-prepared BGs generally increases with their Ca content,^{3,7,9} and that of gel-prepared glasses has been shown to also depend on texture, such as porosity, pore size, and specific surface area.³ The introduction of the sol–gel technique stimulated further exploration of glasses of the CaO–SiO₂ system and the relation between the bioactivity of the glass and its phosphorus content.^{7–13} It was found that although the

presence of P leads to an initially slower formation rate of the amorphous calcium phosphate layer its subsequent crystallization into HCA is promoted.^{3,7,10}

Despite numerous BG material developments, including assessments of their in vitro bioactivities and textual properties,^{1–3,5–13} less attention has been paid to the BG structures over length scales up to a few nanometers. Here, solid-state NMR spectroscopy has been the primary information source, mainly targeted through the local P and Si environments in melt-quenched bioactive and related glasses.^{14–19} A few NMR investigations of sol–gel-prepared BGs have also been reported recently.^{20–23}

An approach to enhance significantly the bioactivity was presented recently by Yan et al.,²⁴ who used a non-ionic surfactant as the structure-directing agent and an evaporation-induced self-assembly (EISA) process²⁵ to prepare *mesoporous bioactive glasses* (MBGs). These materials were developed further by several groups,^{26–30} including the very recent introduction of hierarchical networks that simultaneously involve micro-, meso-, and macropores.^{31,32} Although the MBG bioactivity is, in part, believed to display composition–property relationships similar to those found for melt- and gel-prepared glasses, texture is recognized as being the dominating contribution to the superior in vitro bioactivity, which has been attributed mainly to the highly ordered arrangement of uniformly sized mesopores.^{24,26–29}

MBGs have been prepared with 2D hexagonal (*p6mm*)^{24,26–29} as well as 3D cubic (*Im3d*)²⁸ pore arrangements. Depending on the Ca content of the sample, they are associated with pore diameters between 5 and 10 nm. However, little is known about the MBG structure over length scales up to 10–20 nm. Using scanning and transmission electron microscopy (SEM/TEM) techniques in conjunction with energy-dispersive X-ray spectroscopy (EDS), several groups have independently observed a

* Corresponding author. E-mail: mattias@phyc.su.se. Fax: +46 8 152187. Phone: +46 8 162375.

[†] Physical Chemistry Division, Arrhenius Laboratory, Stockholm University.

[‡] Universidad Complutense de Madrid and CIBER-BBN.

[§] Inorganic Chemistry Division, Arrhenius Laboratory, Stockholm University.

TABLE 1: Compositions of the MBG Samples

sample ^a	batch cation composition (atom %)			experimental cation composition ^b (atom %)			stoichiometric formula ^c	mesoporous structure ^d
	Ca	Si	P	Ca	Si	P		
S58	35.2	55.3	9.5	35.3	56.6	8.1	Ca _{0.62} SiP _{0.14} O _{2.96} (O _{2.99})	<i>p6mm</i> ; disordered
S75	19.1	71.4	9.5	21.2	72.7	6.1	Ca _{0.29} SiP _{0.08} O _{2.49} (O _{2.58})	<i>p6mm</i> ; <i>p2mm</i>
S85	9.5	81.0	9.5	10.3	84.3	5.4	Ca _{0.12} SiP _{0.06} O _{2.27} (O _{2.03})	<i>la3d</i>
S85sbf	9.5	81.0	9.5	8.6	84.8	6.6	Ca _{0.10} SiP _{0.08} O _{2.30} (O _{2.72})	<i>la3d</i>
S100	0	100	0				SiO ₂	<i>la3d</i>

^a Sample notation *Sn*, where *n* represents the nominal mol % SiO₂ in the batch when expressed in oxide equivalents; that is, *x*CaO–*y*SiO₂–*z*P₂O₅. All batches contained an equivalent of 5 mol % P₂O₅ (see ref 28). ^b Measured by X-ray fluorescence (XRF) analysis. ^c Charge-balanced formula, based on the experimental cation composition and normalized with respect to the Si coefficient. The corresponding experimentally XRF-analyzed oxygen coefficient is given within parenthesis. The sample S85sbf also contained small amounts of Na and Cl (0.5 and 0.3 atom %, respectively) and K, Mg, and S in <0.2 atom %. ^d Samples S58 and S75 comprise two separate mesoporous phases, where the major component is listed first. See ref 28 for details.

uniform distribution of Ca, Si, and P over the MBG structure.^{24,26,28,29} Besides the ordered arrangement of mesopores, this “uniform distribution” has partially been used to explain the enhanced MBG bioactivity relative to melt-quenched BGs, which are known to be heterogeneous in their element distribution over tens of nanometers.

However, although the TEM-estimated cation distribution is undoubtedly more uniform for MBG specimens,^{24,26–29} current reports are vague on its precise meaning, particularly in regards to what structural roles Ca and P play with respect to the silica-based pore walls. In this work, we seek to clarify this issue for a series of MBGs having a nearly constant amount of ~6 atom % P (out of the cations) and Ca contents ranging from around 10 to 35%, by exploring their *local* environments using a combination of ²⁹Si, ³¹P, and ¹H magic-angle spinning (MAS) NMR experiments. The set of samples is identical to that reported by López-Noriega et. al. in ref 28 where the MBG structures were investigated by TEM and X-ray diffraction (XRD) and their *in vitro* bioactivities were evaluated. In analogy with previous NMR reports on melt- and gel-prepared BGs,^{14–23} we find that Si and P are separated into *distinct* phases. In the present MBGs, they together constitute the 3–4 nm thick pore wall, which is built primarily by a CaO–SiO₂ glass phase, whereas P is present as an amorphous calcium orthophosphate, presumably dispersed over the pore wall as nanometer-sized clusters. This biphasic MBG structural model implies a high surface accessibility of both Ca and P, which we argue to be a contributing factor to the experimentally observed high MBG bioactivity.^{24,26–28}

2. Experimental Section

Sample Preparation and Characterization. To ensure a direct relevance of the present *structural* study of the MBGs with their previously reported *in vitro* bioactivities, identical synthesis procedures and batch compositions were used as in ref 28. The sample preparation involved an EISA process²⁵ with the non-ionic poly(ethylene oxide)-poly(propylene oxide)-poly(ethylene oxide) [EO₂₀PO₇₀EO₂₀; P123] triblock copolymer as the structure-directing agent, and employing tetraethyl orthosilicate (TEOS), triethyl phosphate (TEP), and Ca(NO₃)₂·4H₂O as the Si, P, and Ca sources, respectively. We refer to ref 28 for details. However, as demonstrated below by our ¹H NMR experiments, the relatively short heating interval of 3 h at 700 °C leaves some residues of organic species that originate primarily from the P123 polymer. We have found that at least 6 h of calcination is necessary to remove all organic moieties.

The amounts of Si, Ca, P, and O were determined by X-ray fluorescence (XRF) using a Philips PANalytical AXIOS wavelength dispersive spectrometer. Following the nomenclature of

ref 28, each MBG specimen is denoted as *Sn*, with *n* being the nominal molar percentage of SiO₂ in the *batch*, which in all cases contained 5 mol % P₂O₅ (9.5 cation % P). See Table 1 for detailed information about the sample compositions. The XRF-analyzed compositions were overall close to those of the batches.

Another specimen (S85sbf) was prepared by immersing S85 MBG powder in SBF for 4 h, as described in ref 28. Additionally, a “reference” mesoporous silica sample (S100) was synthesized under identical conditions as for S85, but omitting TEP and Ca(NO₃)₂·4H₂O. S85 and S100 are isostructural with MCM-48^{33,34} and SBA-16,³⁵ whose bicontinuous mesoporous networks conform to *la3d* symmetry. The Supporting Information (SI) provides textural information about the samples as well as high-resolution TEM micrographs.

Solid-State NMR. MAS NMR spectra were acquired at a magnetic field of 9.4 T on a Varian/Chemagnetics Infinity spectrometer, giving the following Larmor frequencies: –400.17 MHz for ¹H, –161.99 MHz for ³¹P, and 79.50 MHz for ²⁹Si. All experiments were performed on finely ground powders filled in 6 mm zirconia rotors. Single-pulse ²⁹Si and ³¹P experiments were conducted at a spinning speed of 8.5 kHz, except for the ²⁹Si spectra of the S85sbf and S100 samples (7.5 kHz). The acquisitions used 1200 s relaxation delays and 60° pulses (nutration frequency $\omega_{\text{nut}}^{\text{Si}}/2\pi = 27$ kHz) for ²⁹Si experiments and 900 s pulse delays and 70° pulses ($\omega_{\text{nut}}^{\text{P}}/2\pi = 26$ kHz) for ³¹P, with ~200 and 70–160 accumulated signal transients for ²⁹Si and ³¹P, respectively. ¹H single-pulse spectra were recorded at a spinning speed of 9 kHz, using ~1000 transients, 5 s relaxation delays, and 90° pulses ($\omega_{\text{nut}}^{\text{H}}/2\pi = 42$ kHz). Relaxation delays were chosen based on separate *T*₁ saturation recovery measurements for each nucleus.

Ramped cross-polarization³⁶ (CP) ¹H → ³¹P and ¹H → ²⁹Si NMR spectra were recorded at 8.5 kHz spinning frequency (ω_r) with ~4000 transients, using the modified Hartmann–Hahn condition $\omega_{\text{nut}}^{\text{H}} - \omega_{\text{nut}}^{\text{X}} = \omega_r$, (X = Si, P). Typical nutation frequencies were approximately $\omega_{\text{nut}}^{\text{H}}/2\pi = 41$ kHz and $\omega_{\text{nut}}^{\text{P}}/2\pi = 32$ kHz for ¹H → ³¹P CPMAS; $\omega_{\text{nut}}^{\text{H}}/2\pi = 30$ kHz with $\omega_{\text{nut}}^{\text{Si}}/2\pi = 21$ kHz for ¹H → ²⁹Si CPMAS. We verified that applying high-power ¹H decoupling did not improve the ³¹P and ²⁹Si linewidths significantly, and all acquisitions were subsequently performed without decoupling. 2D NMR acquisitions employed time-proportional phase incrementation (TPPI)³⁷ to achieve absorptive-mode spectra with frequency sign discrimination along both frequency dimensions. The remaining experimental details are provided in the figure captions. Chemical shifts are quoted relative to tetramethylsilane (TMS; for ¹H and ²⁹Si) and 85% phosphoric acid (H₃PO₄; for ³¹P).

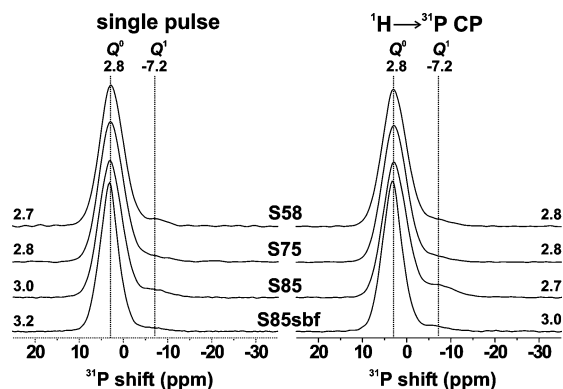


Figure 1. ^{31}P MAS NMR spectra of the MBGs, recorded at 8.5 kHz spinning frequency by direct excitation using single pulses (left panel) and by $^1\text{H} \rightarrow ^{31}\text{P}$ CP with a 4.5 ms contact interval (right column). Numbers at the outermost spectral portions specify the respective peak maxima (in ppm) of the main orthophosphate (Q^0) ^{31}P environment; they are accurate within ± 0.1 ppm.

3. Results

3.1. ^{31}P NMR. Figure 1 shows ^{31}P MAS NMR spectra of the series of MBGs, recorded directly by single-pulse excitation (left column) and by $^1\text{H} \rightarrow ^{31}\text{P}$ cross-polarization (right column). We first consider the spectra from the samples not exposed to SBF. All display a main peak around 2.8 ppm, having a full width at half-maximum height (fwhm) of around 5.3 ppm. Although this chemical shift is the same as that of crystalline calcium hydroxyapatite (HAp),^{38,39} the signal found from the MBGs is significantly broader than that observed from (nano)-crystalline HAp⁴⁰ and is typical for an amorphous calcium orthophosphate phase. The ^{31}P MAS NMR spectra recorded from the present MBGs are very similar to those reported from Ca-rich $(\text{M}_2\text{O})\text{--CaO--SiO}_2\text{--P}_2\text{O}_5$ BGs ($\text{M} = \text{Na}, \text{K}$), wherein a ^{31}P signal appearing around 2.5–3.0 ppm was also attributed to Q^0 environments.^{14–19} The same general conclusions were reached about P in the amorphous surface phosphate layer formed on CaO--SiO_2 glasses on a few hours SBF-exposure.^{21,22}

Onward, we adopt the Q^n notation to denote a phosphorus (or silicon) atom bonded to n bridging oxygen (BO) and $(4 - n)$ nonbridging oxygen (NBO) atoms. The calcium phosphate phase is likely heterogeneous in composition, as pointed out in an NMR study of SBF-exposed BGs.²¹ The Q^0 signal (fwhm 4.1 ppm) of the S85sbf sample is narrower by ~ 1.2 ppm (190 Hz) compared to any of the pristine MBG samples (Figure 1). Although the phosphate phase is still XRD-amorphous in nature,²⁸ the ^{31}P NMR spectrum conveys a slightly increased *local ordering* of the phase after 4 h of exposure to SBF. From Table 1 follows that the P content of the S85sbf specimen is only marginally larger (while the Ca content is even lower) than that of the pristine sample. The ^{31}P NMR peak narrowing may reflect either of two possibilities: (i) a partial *transformation* of the *initially* present calcium orthophosphate component, a majority of which then must be *directly* accessible to fluids, or (ii) the emergence of a *new* SBF-induced phase. Further investigations are required to resolve this: as we noted previously, the phosphate phase present in the MBGs has NMR characteristics very similar to those of the amorphous bioactive phosphate layer formed on CaO--SiO_2 BGs on SBF-exposure,^{21,22} which underlines their local structural similarities.

Besides the signal from the main orthophosphate component, a minor ^{31}P resonance around -7 ppm is present in all spectra; it is most apparent from those recorded from S85 (Figure 1). The position of this minor peak, which is shifted by -10 ppm from that of the Q^0 signal, falls within the range typically found

for ^{31}P in Q^1 tetrahedra,⁴¹ and may as such conform to either of P--O--X ($\text{X} = \text{P}, \text{Si}$) bonding scenarios. Similar ^{31}P signals have been reported occasionally in NMR studies of bioactive glasses.^{16,17,19} Because previous assignments have been rather arbitrary, here we provide a detailed motivation for our attribution of this peak to Q^1 species, which accords with the following observations:

(i) Charge-balancing arguments predict that the number of Q^1 units is expected to decrease as the Ca^{2+} content of the MBG increases. Through deconvolutions of the MAS spectra recorded by direct excitation (Figure 1, left column), we indeed estimated that its contribution diminishes according to: S85 ($\sim 6\%$); S75 ($\sim 4.5\%$); S58 ($\sim 3\%$).

(ii) The resonance of ca. -7 ppm is associated with ^{31}P nuclei experiencing a significantly larger chemical shift anisotropy (CSA) relative those of the more symmetric orthophosphate tetrahedra. This is evidenced by the ^{31}P NMR spectra from S85 (see Figure S2 of the SI), which show that the more shielded ^{31}P nuclei generate more intense spinning *sideband* amplitudes (relative to the centerband) than that of the Q^0 units. The integrated spinning sideband intensities stemming from Q^0 and “ Q^1 ” environments of S85 were compared with numerically calculated amplitudes, as described in ref 42. This leads to the following conservative estimate of the “mean” anisotropy (δ_{aniso}) and asymmetry parameter (η) of the CSA tensor associated with Q^0 units: $\delta_{\text{aniso}}[Q^0] = 27 \pm 4$ ppm and $\eta[Q^0] = 0.7 \pm 0.4$ (using the definitions in ref 42). The value of δ_{aniso} indeed accords with Q^0 environments and is slightly larger than that reported for HAp (~ 17 ppm).^{38,39} The integrated sideband intensities generated from the Q^1 sites could not be satisfactorily fit into a single set of CSA tensor parameters, which underlines that this NMR signal likely originates from several distinct ^{31}P environments. However, the estimated lower bound $|\delta_{\text{aniso}}[Q^1]| > 70$ ppm shows that the “mean” CSA value is more than twice as large as that of the Q^0 ^{31}P nuclei, as is expected from the less symmetric Q^1 units.

(iii) ^{31}P in protonated $\text{H}_n\text{PO}_4^{3-n}$ orthophosphate ions are normally associated with relatively large chemical shift anisotropies between 50 and 70 ppm.³⁸ However, their isotropic chemical shifts are typically appearing > -3 ppm, that is, higher than our observed signal centered at ca. -7 ppm. Furthermore, our ^1H NMR spectra (discussed below) give no hints of ^1H resonances associated with protonated orthophosphates, which normally appear above 8 ppm.⁴³ Also, if initially present, then the sample thermal treatment at 700°C is expected to condense such orthophosphate units into pyrophosphates (e.g., $2\text{HPO}_4^{2-} \rightarrow \text{P}_2\text{O}_7^{4-} + \text{H}_2\text{O}$).

Although the signal at ca. -7 ppm may safely be assigned to ^{31}P in Q^1 units, it is less clear if those derive from P--O--P or P--O--Si bonding scenarios. Similar Q^1 ^{31}P NMR signals have sometimes (rather arbitrarily) been attributed to pyrophosphates (i.e., P--O--P bonds).^{16,19} On the other hand, Lockyer et al. found support for P--O--Si bonding in $\text{K}_2\text{O--SiO}_2\text{--P}_2\text{O}_5$ glasses, based on variations of ^{29}Si chemical shifts for increasing P content of the sample.¹⁷ Our NMR results suggest that the ^{31}P resonance at ca. -7 ppm derives from P--O--Si moieties that stem from a clustering of P at spots of the silica-based pore-wall surface. This conclusion was drawn from the following ^{31}P experimental results on S85, which are discussed in detail in the SI: (i) No ^{31}P signals were detected from *through-bond* $^{31}\text{P--}^{31}\text{P}$ coupling experiments using the refocused 2Q-INAD-EQUATE protocol.⁴⁴ (ii) The ^{31}P double-quantum coherence (2QC) excitation from a series of *through-space* dipolar recoupling experiments employing the R2O_2 pulse sequence⁴⁵

showed overall comparable 2QC buildup rates of the “ Q^0 ” and “ Q^1 ” peaks. Both results strongly disfavor the scenario of significant amounts of P–O–P constellations contributing to the Q^1 ^{31}P peak but leave the possibility of P–O–Si moieties. Then the ^{31}P 2QC excitation must stem from ^{31}P – ^{31}P dipolar contacts between $\text{SiO}_3(\text{OP})$ tetrahedral units clustering at the silica surface.

3.2. ^{29}Si NMR. We employed ^{29}Si NMR to obtain insight into the speciation of the various Q^n silicon-centered tetrahedra present in the MBGs. These materials consist of networks of interconnected SiO_4 units, each one generally bonded to four neighboring tetrahedra (Q^4), as found in the 3D structure of SiO_2 .^{41,46} The surface of mesoporous materials, such as the present bioactive glasses, also involves tetrahedra of lower connectivity than four, that is, Q^3 and Q^2 units, corresponding to $\text{Si}(\text{OSi})_3\text{X}$ and $\text{Si}(\text{OSi})_2\text{X}_2$ environments, respectively, where X is O^- or OH .^{41,46–50} Generally, protons serve as the charge balancing species, that is, $\text{X} = \text{OH}$. Henceforth, $\text{Si}(\text{OSi})_3\text{OH}$ and $\text{Si}(\text{OSi})_2(\text{OH})_2$ tetrahedral units are denoted by Q_{H}^3 and Q_{H}^2 , respectively. However, in the presence of positively charged surface species, either stemming from templating molecules or metal ions as in the present case of Ca-containing MBGs, NBOs may be present as well, that is, $\text{X} = \text{O}^-$. The divalent Ca^{2+} ion may balance either the negative charges of two neighboring $\text{Si}(\text{OSi})_3\text{O}^-$ units or that of one $\text{Si}(\text{OSi})_2(\text{O}^-)_2$ tetrahedron: such silicon environments are labeled Q_{Ca}^3 and Q_{Ca}^2 , respectively.

Figure 2 displays ^{29}Si MAS NMR spectra recorded from the series of MBGs using single-pulse excitation, together with their component lines obtained from spectral deconvolutions. The respective peak positions and relative populations of the Q^n units are listed in Table 2. For the pure silica material S100, the peak assignments are unambiguous and based on that ^{29}Si in Q^4 units generally resonate around -110 ppm, while $8\text{--}12$ ppm ^{29}Si deshielding results from each substitution of a BO atom by a hydroxyl group.^{41,46} As expected, Q^4 units are dominating ($\sim 78\%$), whereas the Q^3 spectral component is present only as a weak shoulder. The chemical shift of each Q^n environment agrees well with that observed from a variety of silica-based materials.^{47–51}

In the case of the Ca-containing MBG samples, the spectral assignments in Figure 2 are less obvious because of the competing roles of Ca^{2+} and H^+ for charge compensation of NBOs and their associated ^{29}Si deshielding.^{41,46} The spectral assignment problem is compounded by the simultaneous increase in the amounts of Ca and surface-adsorbed water, as proven by the ^1H NMR results in the next section. Typical ^{29}Si chemical shifts of Q^n environments in CaO – SiO_2 glasses are reported as follows:^{52,53} Q_{Ca}^3 (-90 ppm), Q_{Ca}^2 (-83 ppm), and Q_{Ca}^1 (-75 ppm); they are representative within ± 4 ppm. We first note that none of the spectra in Figure 2 display significant signal intensity in the region above -75 ppm. Hence, the number of Q_{Ca}^1 units must be low. However, all NMR spectra from the MBGs (Figure 2a–d) evidence non-negligible fractions of Q^3 and Q^2 structural units. These ^{29}Si NMR signals are more prominent in the spectra displayed in Figure 3, which were recorded using $^1\text{H} \rightarrow ^{29}\text{Si}$ CP,^{47–49,54} thereby emphasizing resonances from ^{29}Si in close spatial proximity to protons (i.e., those from surface-residing Q^3 and Q^2 units) compared to the signals from Q^4 environments of the interior of the pore walls. Besides the Q^4 and Q^3 ^{29}Si signals present in all NMR spectra of Figures 2 and 3, those recorded from the two Ca-richest samples S75 and S58 reveal another resonance around -82 ppm, which is readily attributed to Q_{Ca}^2 environments.^{51,52} The same peak assignment has been made previously in the context of

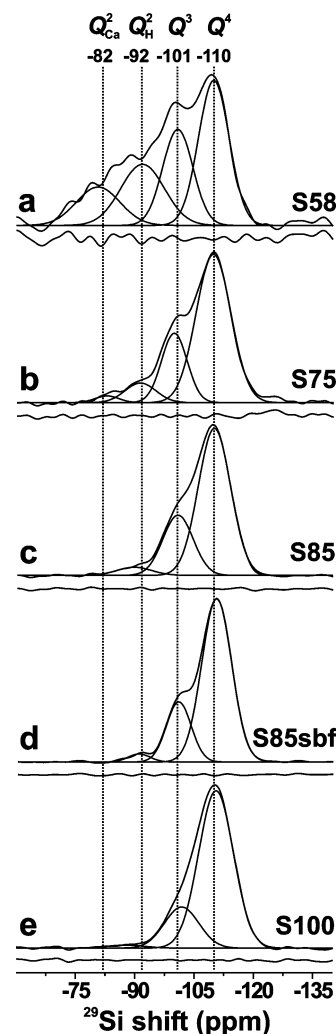


Figure 2. ^{29}Si NMR spectra (black lines) recorded by direct excitation at 8.5 kHz MAS frequency from the set of MBG samples. The peak components as obtained from spectral deconvolutions (see Table 2) are shown by gray lines and assigned to their respective Q^n Si environments as shown at the top. The curve beneath each plot represents the deviation between the experimental and best-fit spectra.

CaO – SiO_2 – P_2O_5 and Ca-rich Na_2O – CaO – SiO_2 – P_2O_5 bioactive glasses.^{14–16,19} As is clear by comparing Figures 2 and 3, the Q_{Ca}^2 signal acquired by $^1\text{H} \rightarrow ^{29}\text{Si}$ CP is emphasized relative to the Q^4 ^{29}Si signals, suggesting that they are in closer spatial proximity to protons than the Q^4 environments of the bulk silicate phase, as discussed further below.

From the trends in the relative populations of Q^n units listed in Table 2, it appears that the amount of Q_{H}^3 tetrahedra (ca. -101 ppm) only grows marginally as the Ca content of the MBG increases and that the reduction in the peak from Q^4 species is primarily associated with a growth of the signals centered around -92 and -82 ppm. This may be rationalized as follows: the introduction of Ca is associated with a concurrently enhanced water adsorption, which leads to an overall increase in the number of hydrogen-bonded SiOH groups. As discussed earlier, the ^{29}Si resonance at ca. -82 ppm stems from Q_{Ca}^2 units, whereas both Q_{H}^2 and Q_{Ca}^3 species resonate around -90 ppm. Hence, this peak carries contributions from both environments. However, the limited Ca content of the MBG specimens (except that of S58) implies that most Ca^{2+} ions are consumed in the formation of the phosphate phase, which readily explains why the NMR signal from Q_{Ca}^2 units is significant only in the ^{29}Si spectrum from S58.

TABLE 2: ^{29}Si Chemical Shifts and Relative Populations of Q^n Units

sample	Q^4		Q^3		Q^2 (Q^3_{Ca}) ^a		Q^2_{Ca}	
	δ/ppm^b	population(%) ^b	δ/ppm	population(%)	δ/ppm	population(%)	δ/ppm	population(%)
S58	-110.0	38	-100.9	25	-92.0	23	-80.8	14
S75	-109.9	67	-100.0	23	-91.5	8	-83.0	2
S85	-110.2	69	-101.0	27	-89.9	4		
S85sbf	-110.7	75	-101.2	23	-91.1	2		
S100	-110.5	78	-101.9	20	-87.8	2		

^a In the case of the Ca-containing samples, Q^3_{Ca} units also contribute to this resonance. ^b ^{29}Si chemical shifts δ (accurate within ± 0.5 ppm, except for S58: ± 1 ppm) and relative populations of the given Q^n unit (accurate within ± 4 percentage units), as obtained by deconvoluting the experimental spectra of Figure 2 by an iterative fitting procedure.

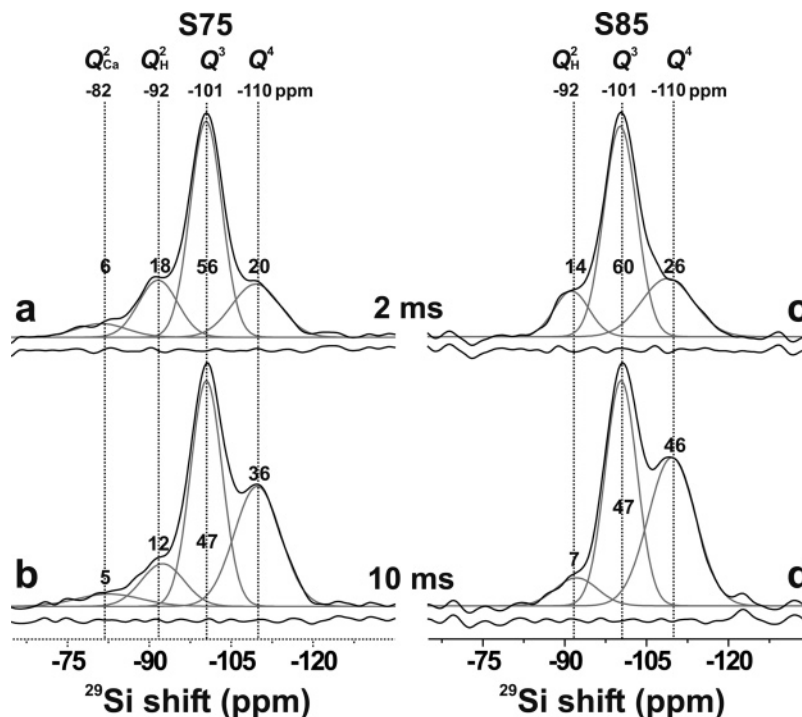


Figure 3. $^1\text{H} \rightarrow ^{29}\text{Si}$ CPMAS NMR spectra (black lines) recorded from S75 (a and b) and S85 (c and d) MBG samples at 8.5 kHz spinning frequency. CP contact intervals of 2 ms (a and c) and 10 ms (b and d) were used. The component peaks obtained from spectral deconvolutions are displayed by gray lines, and each integer put just above (or inside) each component peak represents its relative integrated intensity in %. The difference between experimental and best-fit spectra is shown beneath each plot. Note the emphasized signals from ^{29}Si in close proximity to ^1H , i.e., from the surface-associated Q^2 and Q^3 silicate units, relative to the respective contribution of the Q^4 environment (compare with Figure 2).

The nonlinear trends in the relative populations of Q^2 and Q^3 units against an increasing Ca MBG content (see Table 2) suggest that the NBOs accompanying the Ca^{2+} ions are *not shared equally* between Si and P tetrahedra. As discussed further below, significantly lower amounts of Q^3 and Q^2 silicate environments (regardless of whether H^+ or Ca^{2+} acts as charge compensator) are observed from the MBGs than those expected from a continuous network of intimately mixed SiO_4 and PO_4 units and incorporating all Ca^{2+} ions. Altogether, the ^{31}P and ^{29}Si NMR results strongly point toward a *biphasic* structural scenario, where one $\text{CaO}-\text{P}_2\text{O}_5$ component is characteristic of Q^0 units, that is, associated with a *minimum* network connectivity, whereas, the connectivity of the silica-based network is *maximized*; that is, Q^4 and Q^3 units dominate.

3.3. 1D ^1H NMR. ^1H MAS NMR was used for investigating the nature of the MBG surface through its various proton environments present as SiOH groups and adsorbed water. It has been argued that surface silanols play a decisive role for glass bioactivity because they act as nucleation sites for HCA formation.^{2,3}

The ^1H chemical shift depends primarily on the H-bonding strength, that is, on the $\text{OH}\cdots\text{O}$ distance.^{41,43,55} The number of protons accessible to hydrogen bonding in turn depends on the

extent of physisorbed water. The various types of proton surface environments may be classified broadly as follows: “isolated” SiOH groups are not hydrogen-bonded to either water molecules or other silanols and resonate between 1.5 and 2 ppm.^{47,49,50,56–62} Signals from weakly H-bonded species (observed from relatively dehydrated surfaces) appear between 3 and 4 ppm, whereas more extensive hydrogen bonding is reflected in more positive chemical shifts: the strongest H-bonded silanols are characterized by very broad ^1H signals around 6–8 ppm.^{47,49,50,57–62} For example, NMR studies of the SBA-15 and MCM-41 hexagonal mesoporous materials have shown that the ^1H peak position associated with weak or moderately strong H-bonding varies smoothly between 3 and 5 ppm, depending on the amount of surface-bound water.^{57,60,61} Recent work has demonstrated that its chemical shift can be modeled as a weighted average, based on a rapid proton exchange among sites corresponding to both isolated and hydrogen-bonded silanols as well as water.^{57,58}

Figure 4 displays ^1H NMR MAS spectra recorded from the MBG samples at a spinning rate of 9.0 kHz. All spectra, except that of S85sbf, share the same set of peaks, which differ mainly in their amplitudes. The peak assignments are compiled in Table 3; each resonance is labeled by a letter (A, B, etc.) and will be discussed throughout this section. All NMR spectra comprise a

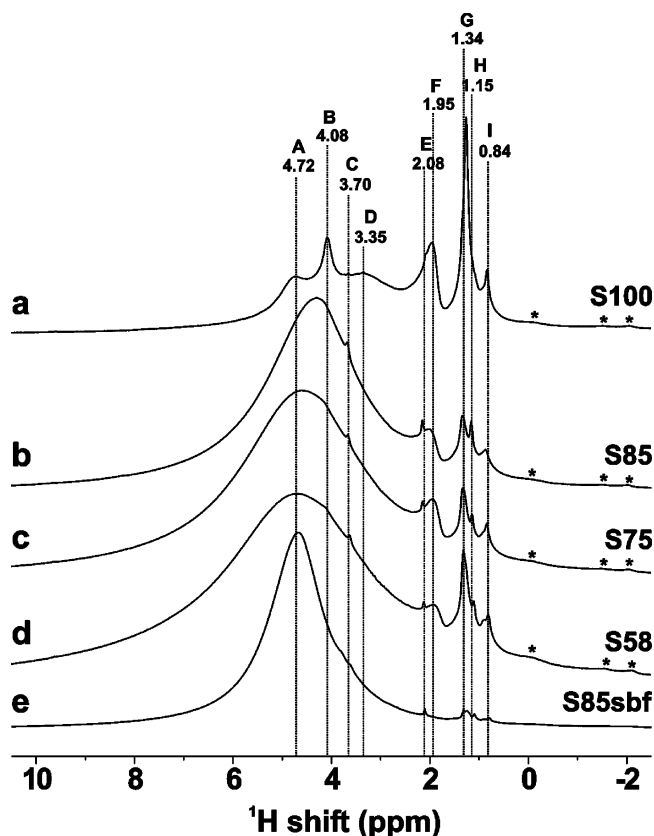


Figure 4. ^1H NMR spectra recorded at 9.0 kHz MAS frequency. The peak assignments (A–I) are explained in Table 3. Asterisks mark background signals (verified from a separate acquisition using an empty rotor).

TABLE 3: ^1H NMR Peak Assignments^a

label	chemical shift (ppm) ^b	feature	assignment ^c
A	4.3–5.0 ^d	broad	physisorbed water
B	4.1	narrow	OCH_2 (TEOS)
C	3.6–3.7	narrow	OCH_2 (P123)
D	3.2–3.9 ^d	broad	SiOH , weakly H-bonded
E	2.1–2.2	narrow	SiOH , isolated
F	1.90–2.00	narrow	SiOH , isolated
G	1.25–1.35 ^e	narrow	CH_3 (TEOS)
H	1.15–1.20 ^e	narrow	CH_3 (P123)
I	0.75–0.85 ^e	narrow	CH_3 (P123)

^a Peak labels refer to those in Figure 4. ^b The accuracy/reproducibility of the shift referencing is within ± 0.03 ppm. ^c Assignments of the organic groups as P123 and TEOS sources are tentative. ^d The precise peak position depends on the water content of the mesoporous surface. ^e The net signal has several underlying minor components over the indicated ranges.

main signal A, which broadens and moves to higher chemical shifts as the Ca content of the sample increases. This is most evident when comparing the peak maximum from S85 (4.3 ppm) and S58 (4.7 ppm) and noting that the fwhm ~ 4 ppm of the signal from S58 is 1.6 times broader than that of S85. This resonance is attributed to ^1H experiencing moderately strong hydrogen bonding, primarily involving physisorbed water molecules.^{47,49,50,57,58} Because our main objective was to identify the various MBG ^1H environments potentially present at different surface hydration levels rather than their precise quantitation, our work did not employ airtight sample holders during the NMR experiments. However, it should be noted that all MBG spectra presented in Figure 4 were recorded from freshly packed samples that were stored under identical conditions (sealed plastic bags in room temperature) prior to measure-

ments. MAS is known to dehydrate the silica surface.⁴⁹ This was indeed observed on continuous sample spinning over several days and manifested by a reduction of the intensity of peak A and the concurrent increase in the signals around 2.0 ppm (labeled E and F); the latter are attributed to “isolated” SiOH groups.^{47,49,50,57–62} Similar NMR peaks from two distinct isolated silanols were reported recently in a silica-based material.⁶²

Besides the MBG surface proton signals A, E, and F, all ^1H NMR spectra display a set of very narrow resonances (typically fwhm < 40 Hz) appearing between 0.8 and 1.3 ppm (peaks G, H, and I). They originate from highly mobile methyl groups, stemming primarily from polypropylene oxide segments in residues of the block polymer P123.⁶¹ Solution NMR studies of P123 have shown that the precise positions of its ^1H resonances depend on both the sample hydration level and temperature (molecular mobility).⁶³ The corresponding OCH_2 signals from P123 are discernible as a narrow peak appearing in all spectra at 3.7 ppm (C).⁶¹ However, the varying NMR peak intensities of G, H, and I between the spectra suggest the presence of a diversity of similar, yet distinct, organic species. We note that all three precursors involved in the synthesis (P123, TEOS, and TEP) are associated with OCH_2 and CH_3 functional groups. TEOS is reported to give OCH_2 and CH_3 ^1H signals around 4.0 and 1.5 ppm, respectively.⁶⁴ Hence, the peaks at 4.1 ppm (B) and 1.3 ppm (G) are attributed to TEOS residues. These assignments are tentative but are suggested further by the simultaneous emphasis of peaks B and G in the ^1H NMR spectra of S100 and S58 relative to the others.

Peak A is weak in the spectrum of S100. This reflects a relatively dehydrated silica surface due to the absence of Ca in this sample. The diminished signal A reveals another broad resonance between 3 and 4 ppm, labeled D and attributed to weakly hydrogen-bonded silanols.^{57,60,61} This peak is present also in the MBG ^1H NMR spectra and is emphasized on removal of the protons associated with signals A, B, and C by heat treatment, as discussed in the SI.

Although the signals of organic species complicate ^1H spectral interpretations, we used the same relatively short calcination intervals as in ref 28 to ensure comparability with that study. The organic species-deriving peaks are emphasized in ^1H NMR spectra because of their very narrow widths relative the other signals. However, the contributions from residual organic molecules are not large in the samples: elemental analysis of S85 and S58 indicated very similar carbon contents of ~ 1 wt %. Furthermore, by ^1H spectral deconvolutions we estimated the fractions of protons present in organic groups as 6% (S85) and 2% (S58). An approximate upper limit of the reduced active surface area due to organic species was estimated to be $\sim 7\%$, based on an assumption of ethoxy residues with a penetrating depth of ~ 0.5 nm into the pore wall. This depth depends on the degree of microphase separation between P123 molecules and silica, which is dependent on the reaction conditions.⁵¹

3.4. Double-Quantum ^1H NMR. The various MBG ^1H environments were also probed according to their through-space dipolar interactions and associated relative internuclear distances using the POST-C7 dipolar recoupling sequence for ^1H 2QC excitation.⁶⁵ A progressively increased dipolar recoupling interval leads to a 2QC signal buildup, whose rate depends on the (motionally averaged) ^1H – ^1H dipolar interaction within a pair of interacting protons; the fastest 2QC excitation occurs between rigid ^1H in close spatial proximity ($\lesssim 0.5$ nm), whereas a slower buildup is observed from a pair associated with high mobility and/or a long internuclear distance. The results obtained from S85 (see Figure S5 in the SI) evidence that the protons of

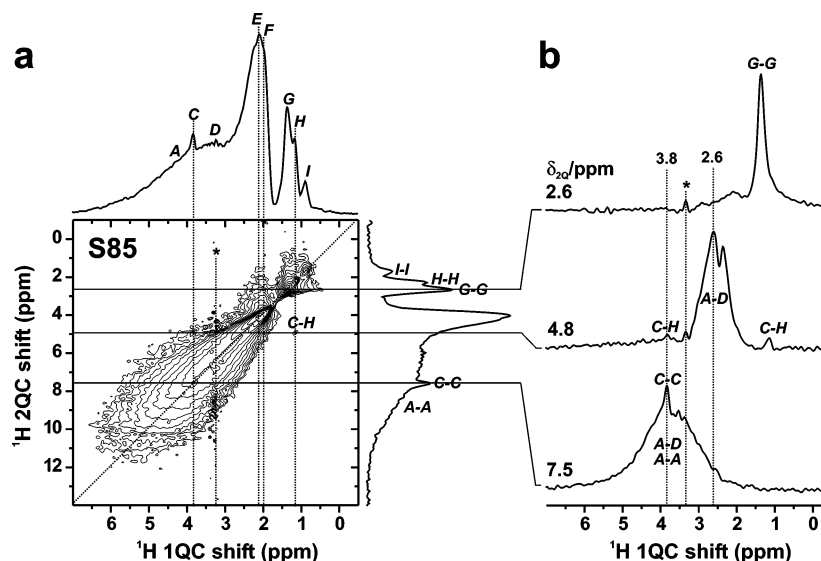


Figure 5. (a) 2QC–1QC ^1H – ^1H correlation spectrum of S85, recorded at 9.0 kHz MAS frequency and using 444 μs POST-C7 recoupling intervals for 2QC excitation and reconversion. The top 1D spectrum shows the 1QC projection, with each resonance labeled as in Figure 4 and Table 3. The projection along the 2Q (vertical) dimension is displayed to the right, where the identified autocorrelation peaks (involving 2QC between equivalent protons) are marked. They appear along the diagonal of the 2D spectrum. (b) A selection of slices through the as indicated constant 2QC frequencies δ_{2Q} . Note that these values are sums of the respective correlated 1Q frequencies. Some tentatively identified signal correlations are indicated in each slice. The peak marked by an asterisk in a and b is a carrier frequency artifact. 2D contour levels are set between 4% and 93% of the maximum intensity. 2D acquisition parameters: $230(t_1) \times 850(t_2)$ time points were acquired, zero-filled to 512×2048 points prior to 2DFT; $\Delta t_1 = 71.43 \mu\text{s}$; $\Delta t_2 = 55.56 \mu\text{s}$; 112 transients/ t_1 value; 4 s relaxation delays.

organic CH_x moieties (peaks **G–I**) and the H-bonded $\text{H}_2\text{O}/\text{OH}$ groups associated with signal **A** provide the fastest 2QC buildup, the latter possibly involving 2QC with the protons giving signal **D** (see below). However, as observed in the context of T_2 relaxation through spin–echo experiments (see the SI), peak **A** also displays the fastest decay, which depletes the signal region >4 ppm for recoupling intervals beyond 0.5 ms. As expected, the isolated SiOH groups (peaks **E** and **F**) manifest the slowest 2QC signal buildup. These results further support each ^1H peak assignment.

Figure 5 shows a ^1H 2QC–1QC correlation NMR spectrum recorded from S85 on application of 0.44 ms 2QC excitation interval. Such a 2D spectrum reveals *qualitative* ^1H – ^1H internuclear proximities because the 2QC frequency (vertical dimension) of a pair of protons is correlated with its respective single-quantum resonances along the horizontal dimension. The spectrum shows autocorrelation peaks (**G–G**, **H–H**, **I–I**) for each of the three resolved CH_3 signals as well as weak 2QC signals involving the CH_3 (**H** ≈ 1.15 ppm) and OCH_2 group (**C** ≈ 3.7 ppm) of the P123 polypropylene segments. The latter observation confirms the previous assignments of these peaks. The spectral features >2.5 ppm in the horizontal 1QC dimension (>5 ppm in the vertical 2QC dimension) are less straightforward to interpret because of severe overlap between signals from protons **A** and **D**, which hampers the distinction of the potential **A–A**, **D–D**, and **A–D** 2Q coherences. We tentatively assign the two ridges spreading around the autocorrelation diagonal between 2 and 4 ppm in the 1QC dimension to **A–D** correlations; they are most clearly seen in the slice $\delta_{2Q} = 4.8$ ppm in Figure 5b. Furthermore, most signal intensity $\delta_{2Q} > 8$ ppm is likely originating from **A–A** autocorrelations.

3.5. 2D Heteronuclear Correlation NMR. HETCOR NMR experiments were performed to get further insight into the relative spatial proximities between the various ^1H and X environments ($X = ^{29}\text{Si}$, ^{31}P), using CP for magnetization transfer. Such 2D HETCOR spectra reveal only X resonances (horizontal dimension) from nuclei in close proximity to protons, whose signals appear along the vertical dimension.^{21,40,48,50,51,58,66}

Figure 6a depicts a ^1H – ^{29}Si HETCOR spectrum of S100. From the projection of the 2D spectrum along the ^1H chemical shift dimension, it is clear that primarily three distinct ^1H environments constitute magnetization sources for each of the Q^2 , Q^3 , and Q^4 ^{29}Si tetrahedra. Those are, as expected, involving silica surface protons, namely isolated silanols (**F** ≈ 2 ppm), the weakly H-bonded silanols (signal **D** ≈ 3.3 ppm), and the more strongly H-bonded groups constituting $\text{SiOH}/\text{H}_2\text{O}$ (**A** ≈ 4.3 ppm). The corresponding HETCOR result from the MBG sample S85 is shown in Figure 6b. Here the main magnetization sources for ^{29}Si are the protons associated with signal **A** and the isolated silanols **F**. Although the weakly hydrogen-bonded silanols **D** likely also give contributions, they are significantly less than those for S100. This is for instance clear when comparing the ^1H slices through the ^{29}Si Q^3 signals at -101 ppm in Figure 6c and e. The Q^3 silicate units in S100 receive most of their cross-polarized signal from protons of peak **D**, whereas those in S85 draw most of their magnetization from the ^1H associated with peak **A**. However, this naturally stems from the overall higher amounts of physisorbed water at the S85 surface compared to that of S100; potential contributions from **D** are obscured by the dominating signal **A** in Figure 6b, as for all MAS spectra of Figure 4, except that of S100. Furthermore, the 2D acquisition of S85 used fewer t_1 samplings in the indirect ^1H dimension, which somewhat compromised the spectral resolution.

Figure 7 shows a ^1H – ^{31}P HETCOR spectrum recorded of S85. Because of a rapid ^1H signal decay during t_1 evolution, the spectral resolution in the ^1H dimension is limited. Although this unfortunately prevents detailed conclusions (as well as the application of potentially more informative HETCOR-based experiments⁵⁰), it is clear that the primary ^{31}P magnetization source stems from a ^1H signal ~ 4.5 ppm, which is attributed to physisorbed water. ^1H signals from structural water of calcium phosphates are usually appearing >5 ppm.^{21,40,43,66} Most remarkable is the correlation of ^{31}P in Q^0 units with a ^1H signal ~ 0.3 ppm. The latter is characteristic of the OH environments in HAp.^{21,40,43,66} This suggests that the amorphous calcium

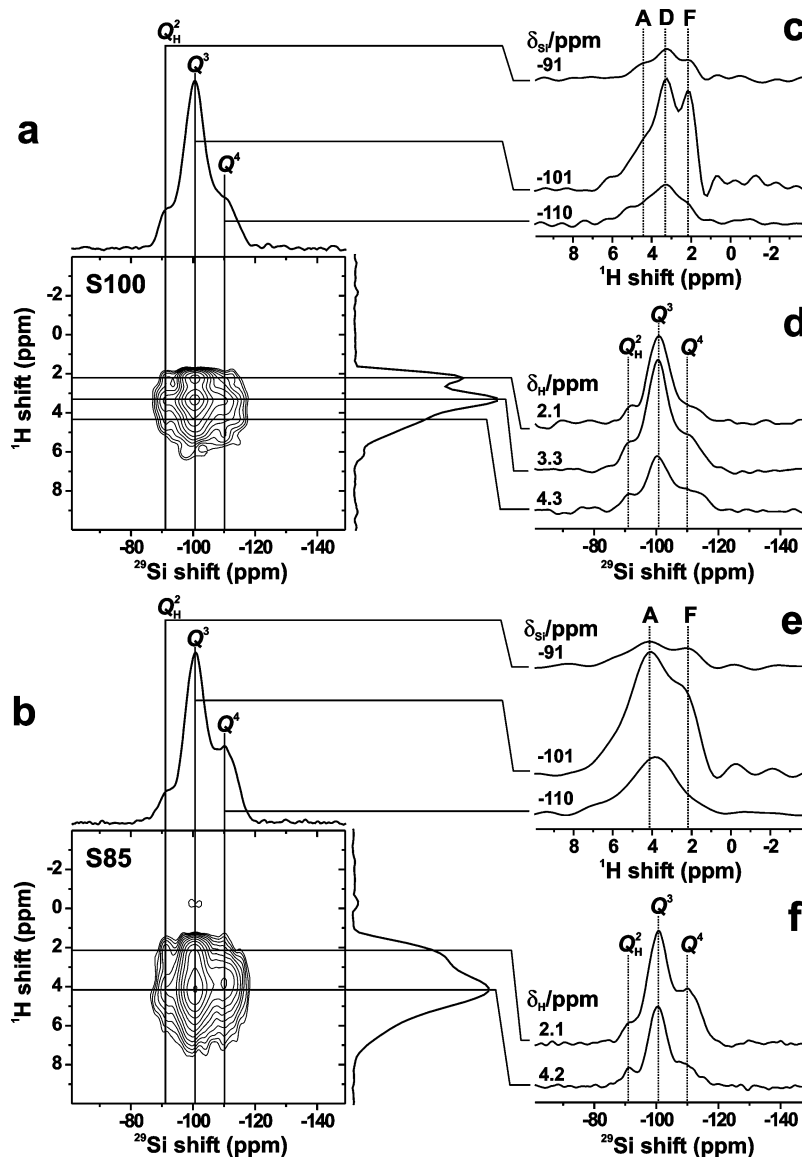


Figure 6. 2D ^1H – ^{29}Si HETCOR NMR spectra recorded from (a) S100 and (b) S85 at 7.5 kHz MAS frequency. 1D projections along the ^{29}Si (horizontal) and ^1H (vertical) spectral dimensions are shown at the top and right of each 2D spectrum, respectively. A selection of slices are displayed in c–f, taken through the 2D spectra at the position of each gray line. The peak labels at the top of the spectra in (c, e) and (d, f) refer to those of Figures 4 and 2, respectively. 2D contour levels are displayed from 6% of the maximum peak intensity. 2D acquisition parameters: 4.53 ms CP contact interval; 4 s relaxation delays; (a) 38 and (b) 28 t_1 (^1H) time points with 220 t_2 points (^{29}Si) were acquired and zero-filled to a 128×1024 data set prior to 2DFT; $\Delta t_1 = 66.67 \mu\text{s}$, $\Delta t_2 = 44.44 \mu\text{s}$; 1664 (a) and 1984 (b) signal transients were accumulated per t_1 value.

orthophosphate phase comprises minor amounts of OH groups, similar to those found in HAp. Because of the very low P content of the sample, this ^1H resonance is expected to be very weak in directly detected MAS NMR spectra and is obscured by background signals in this spectral region.

4. Discussion

MBG Structural Model. This section summarizes the NMR results on the local ^{29}Si and ^{31}P environments, which are discussed and combined into an MBG pore-wall model that expands on the current structural understanding by complementing it over a length scale up to a few nanometers.

4.1. Silica and Phosphate Components. Unarguably, the pore wall is based primarily on the silica phase.^{24,26–30} We further note that our ^{31}P and ^{29}Si NMR data unambiguously show that the majority of P is not intimately intermixed with Si but rather present in a separate amorphous calcium orthophosphate phase. Onward we disregard the <6% of P present as Q^1 units, where phosphorus is probably anchored at the

mesoporous surface through Si–O–P linkages (see the SI). This minor P constituent has little, if any, bearing on the MBG bioactivity. The structural role of P in the MBGs is on an atomic scale expected to be similar to that in gel- and melt-prepared BGs, which display a lower in vitro bioactivity, that is, slower HCA formation on SBF exposure. Hence, the enhanced MBG bioactivity *must* result primarily from longer-range structural/textural effects, as *expected*.^{24,26,28,29} The most important factor is the greatly enhanced surface area of the MBGs relative to BGs.^{24,26–29} The “homogeneous cation distribution” is also contributing; however, although we have unambiguously shown that the P and Si distribution is *heterogeneous* on an atomic length scale, we will in the following discussion clarify the MBG structural picture. This model leads to a high *accessibility of Ca and P at the MBG surface* through a close association of the two CaO – SiO_2 and CaO – P_2O_5 pore-wall components.

Calcium is required for forming the amorphous orthophosphate phase, whose precise composition is unknown; however,

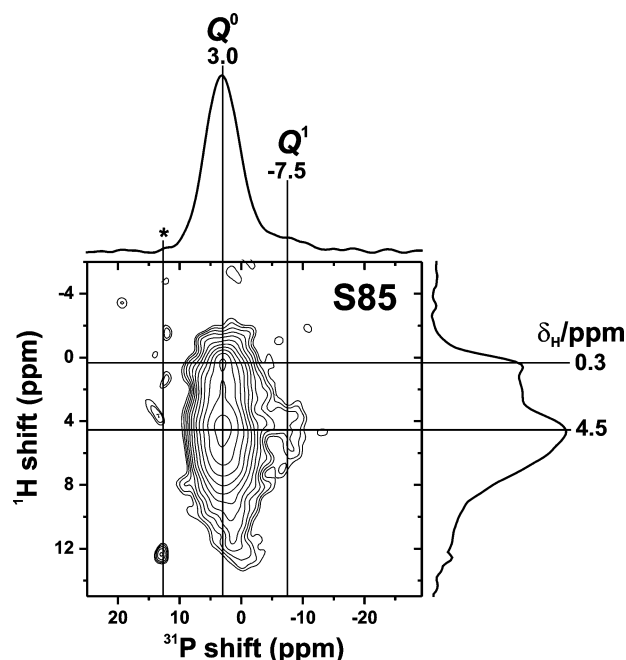


Figure 7. ^1H – ^{31}P HETCOR NMR spectrum of S85 recorded at 9.0 kHz MAS frequency. The 2D spectrum is shown together with its projections along each spectral dimension. Only the spectral region comprising signals is shown, with 2D contour levels ranging between 5% and 90% of the maximum peak intensity. The ridge along $\delta_{\text{P}} \approx 13$ ppm (marked by an asterisk) stems from a probehead artifact signal of unknown origin. The 2D acquisition used a 1.89 ms CP contact interval, $50(t_1; ^1\text{H}) \times 300(t_2; ^{31}\text{P})$ time points with $\Delta t_1 = 55.56 \mu\text{s}$, $\Delta t_2 = 27.78 \mu\text{s}$, 384 transients/ t_1 value, 4 s relaxation delays, and zero-filling to 128×1024 points prior to 2DFT.

it is reasonable to assume a Ca/P ratio between that of $\text{Ca}_3(\text{PO}_4)_2$ (Ca/P = 1.50) and HAp (Ca/P = 1.67), particularly when considering the indication from ^1H – ^{31}P HETCOR NMR of some P–OH groups present in this phase. Assuming a stoichiometric nominal $\text{Ca}_3(\text{PO}_4)_2$ composition, the phosphate phase consumes essentially all Ca in the S85 sample, and roughly $1/2$ and $1/3$ of the total Ca supply in the case of S75 and S58, respectively. The remaining CaO is available for defragmenting the silica glass network, which constitutes almost pure (amorphous) silica in the case of S85, and a silica-rich CaO – SiO_2 glass phase of nominal approximate composition $\text{Ca}_{0.2}\text{SiO}_{2.2}$ and $\text{Ca}_{0.4}\text{SiO}_{2.4}$ for S75 and S58, respectively. The domination of high-connectivity Q^4 and Q^3 species as derived from the ^{29}Si MAS spectra (Table 2) is consistent with such silica-rich networks, but *incommensurate* with an *equal* distribution of the NBO atoms among SiO_4 and PO_4 units (compare, for example, the ^{29}Si NMR spectra of Figure 2 with those from the CaO – SiO_2 glasses in ref 20).

Our ^{29}Si NMR data do not directly disclose the preferential connectivities between the various Q^n silicate units. However, given the large surface area, the most natural structural scenario is that of an essentially pure SiO_2 network in the interior of the 3–3.6 nm thick pore wall (see Table S1 of the SI), whereas the units associated with lower connectivities (i.e., Q_{H}^3 , Q_{Ca}^3 , Q_{H}^2 , and Q_{Ca}^2) are located at/near its surface. This leads to a gradient in the Ca concentration across the wall.

We stress that our present set of experimental data cannot unambiguously prove an enhanced Ca concentration at the mesoporous surface. Nevertheless, all of our results point toward it, and a similar remark on the role of Ca was made recently in the context of gel-prepared BGs.²² First consider the $^1\text{H} \rightarrow ^{29}\text{Si}$ CPMAS NMR spectra of S75 (Figure 3a and b): the peak

associated with Q_{Ca}^2 is emphasized relative to that in Figure 2b (compare the relative integrals of Table 2 and Figure 3 for the S75 spectra). More importantly, however, is its significant enhancement relative to the Q^4 tetrahedral units in Figure 3a. This spectrum was recorded with a relatively short contact interval, thereby ensuring that the various ^{29}Si signal intensities are less influenced by damping effects stemming from relaxation processes and ^1H spin diffusion during CP. These observations support that the Q_{Ca}^2 peak stems primarily from *surface* silicate units because the magnetization source of ^{29}Si may only originate from surface-associated ^1H , that is, either SiOH groups or adsorbed water. The hydroxyl groups present in the pore-wall interior are expected to be comparatively minor.⁵⁶ Comparison of the relative signal contributions to the spectra from S75 shown in Figures 2 and 3 shows that although the ^{29}Si signals from the surface-associated Q_{Ca}^2 , Q_{H}^2 , and Q_{H}^3 environments are all emphasized relative to those of the Q^4 units the enhancements are largest for the Q_{H}^2 and Q_{H}^3 tetrahedra that involve OH groups, as opposed to the ^{29}Si of the Q_{Ca}^2 units that cross-polarize from more distant ^1H at the surface. Also note the *absence* of similar Q_{Ca}^2 signals in the spectra of Figure 3c and d, in agreement with the earlier postulated near-absence of Ca in the silica-based pore-wall part of the *Ca-poor* S85 sample. Next, a tendency of Ca to cluster at/near the surface also accords with the broadened ^1H signal A ≈ 4.7 ppm from S58 relative to that of S85 (compare Figure 4b and d). This signal was attributed to involve primarily adsorbed water (Table 3), and its increase with the Ca content is obvious in Figure 4. Most important, the Ca-clustering at the silica surface naturally lends itself to a high accessibility to diffuse and react with body fluids, thereby contributing to the enhanced HCA formation rate as observed experimentally *in vitro* for MBG samples relative to that from previous bioactive glasses.^{24,26–29}

4.2. Pore-Wall Structure. A remaining question is the relation between the CaO – P_2O_5 and (CaO) – SiO_2 structural constituents. The various possibilities may be classified broadly as follows: (A) the two phases are *macroscopically* separated. This scenario may safely be ruled out from the homogeneous distribution of Ca, Si, and P found from TEM/EDS.^{24,26,28,29,32} The instrumentation used in ref 28 may for these materials ascertain a homogeneous cation distribution over a length scale $\gtrsim 20$ nm. This leaves the only feasible scenario that the calcium orthophosphate phase must be closely associated with the MBG *pore wall*, either dispersed over its surface as *adsorbed* clusters or in the form of a noncontiguous layer (case B) or present as *inclusions* within the pore wall itself (case C, depicted in Figure 8).

For the present MBGs, either scenario B or C is consistent with the TEM/EDS observations²⁸ as well as with the following NMR-based results of the present work, which implies a high surface accessibility of the CaO – P_2O_5 phase: The Q^0 signal in ^{31}P spectra recorded by $^1\text{H} \rightarrow ^{31}\text{P}$ CPMAS (requiring a close proximity to ^1H) is within experimental error essentially identical in both its mean peak position and fwhm compared to the corresponding MAS spectra obtained by *direct* excitation (Figure 1). Because the latter *quantitatively* reflects the *total* P content of the sample, the CPMAS spectra show that most P atoms must be within close ($\lesssim 0.7$ nm) spatial proximity to the protonated species. These ^{31}P results may be contrasted with those for ^{29}Si in Figures 2 and 3, which display strikingly different ^{29}Si Q^n populations as obtained quantitatively from each sample by direct excitation and from CP that emphasizes surface units. We further argue that, as for the location of the Ca ions, the MBG bioactivity is expected to increase if most of the P atoms

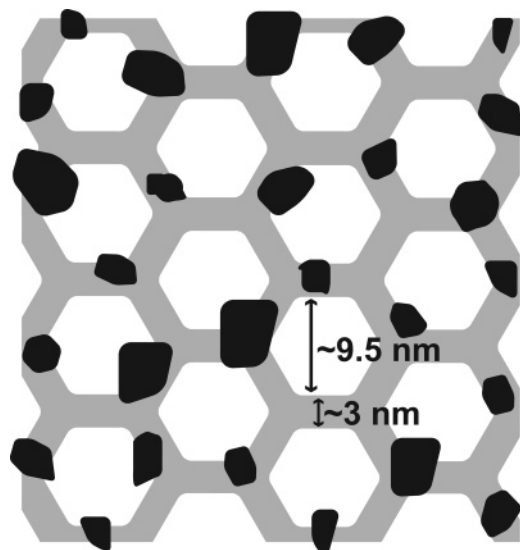


Figure 8. Proposed MBG structural model, with the main CaO-SiO_2 -based amorphous pore-wall component displayed in gray, comprising nanometer-sized “inclusions” of the calcium orthophosphate phase (black regions). The indicated dimensions of the pores and pore walls are representative for the Ca-richest MBG S58 (see Table S1 of the SI). The only essential differences to the S75 and S85 specimens are their slightly thicker pore walls (~ 3.5 nm) and their lower amounts of Ca in the silica-based constituent.

are easily accessible to body fluids, that is, present at/around the MBG surface. This statement accords with the results of ref 29, as discussed further below. Although neither previous TEM/SEM studies nor the present NMR investigation may readily distinguish the structural scenarios *B* and *C*, we note that the latter is more probable when considering previously proposed models involving phosphate clusters in the case of sol-gel BGs.⁵ Hence, we favor the location of the calcium orthophosphate phase as being a pore-wall constituent (i.e., model *C*). It is presumably present as nanometer-sized clusters disrupting the main silica-based network, as shown in Figure 8. The distribution of cluster sizes is unknown but is most likely confined between 2 and 5 nm. This statement is based both on upper experimental constraints provided by TEM/EDS and by the pore diameters themselves (Table S1). On the other hand, the mean ^{31}P NMR chemical shift, incidentally very similar to that observed from bulk HAp, is suggesting cluster sizes of at least a few nanometers, in order not to emphasize shift contributions from P tetrahedra present at the cluster boundaries, whose ^{31}P chemical shifts are expected to be different from those of units found in the interior of the cluster.

In summary, we propose a model of a main $(\text{CaO})\text{-SiO}_2$ pore-wall component, interleaved with calcium orthophosphate clusters, presumably of comparable sizes as the thickness of the pore wall (see Figure 8). Furthermore, the Ca ions of the CaO-SiO_2 phase are associated primarily at its surface. Altogether, besides the widely accepted contribution from surface silanols,^{2,3} this structural model provides natural nucleation spots for the growth of the amorphous calcium phosphate clusters on body fluid exposure. It was demonstrated recently that the MBG bioactivity could be enhanced further, as opposed to the case of gel-prepared BGs, by mixing the MBG glass powder with a $(\text{NH}_4)_2\text{HPO}_4$ solution.²⁹ The promoted HCA formation rate was attributed both to the presence of HPO_4^{2-} ions as well as to a rapid release of Ca^{2+} from the MBG surface.²⁹ All of this is consistent with the structural model presented here, where the Ca and P association at the MBG surface *inherently* provides their enhanced availability to body

fluids relative to that of the less-ordered BGs. Similarly, we argue that the MBG cements²⁹ exploit this structural property further for improving the bioactivity.

5. Conclusions

This work complemented the nanometer/micrometer structural picture of highly ordered mesoporous bioactive $\text{CaO-SiO}_2\text{-P}_2\text{O}_5$ glasses as derived from TEM/SEM^{24,26–29} by combining the atomic-scale information accessible from ^1H , ^{29}Si , and ^{31}P 1D MAS NMR (revealing the immediate nuclear environments over $\lesssim 3\text{Å}$) with that obtained over a range $\lesssim 6\text{Å}$ from homonuclear $^1\text{H-}^1\text{H}$ and $^{31}\text{P-}^{31}\text{P}$ double-quantum NMR and heteronuclear ($^1\text{H-}^{29}\text{Si}$ and $^1\text{H-}^{31}\text{P}$) cross-polarization-based correlation experiments.

Our results have amounted in a proposed two-component MBG pore-wall model, involving a main silica-glass phase, which carries inclusions of nanometer-sized amorphous calcium orthophosphate clusters. The silicate network is to a minor degree modified by the Ca^{2+} ions not consumed when forming the calcium phosphate phase. However, only the Ca-richest sample S58 (35 atom % Ca out of the cations) displayed clear signs of network defragmentation, through the presence of a noticeably increased amount of Q^2 silicate tetrahedra. This pore-wall model accords with all ^{31}P , ^{29}Si , and ^1H NMR results of the present study as well as with the observed even distribution of cations over the TEM/SEM-accessible length scales from tens of nanometers to the micrometer range.^{24,26,28,29,32} As opposed to the case of previous BGs, the higher MBG surface area in conjunction with a more homogeneous distribution of Ca and P near the MBG surface may be a possible explanation for the experimentally observed enhanced MBG bioactivity^{24,26–29} through a facilitated access of all cations to fluids. This provides a natural scenario of surface nucleation sites for further growth of the amorphous calcium phosphate clusters into a layer and its subsequent crystallization into HCA.

^1H NMR revealed surface-associated ^1H environments of water molecules and various hydrogen-bonded and “isolated” SiOH groups. A correlation was observed between an increasing amount of surface-adsorbed water as the Ca content of the MBG specimen increased. The simultaneous enhanced concentration of surface silanols is likely also a contributing factor to the high MBG bioactivity;^{2,3} indeed, the formation rate of the initially amorphous apatite layer has been shown to be higher in vitro for S58 compared to S85.²⁸

In conclusion, the pore-wall structural model presented here is more subtle than a mere “homogeneous cation distribution”,^{24,26,28,29,32} while also complying with our observation that the *local* ^{29}Si and ^{31}P environments in the MBGs are similar to those reported previously for bioactive glasses prepared by melt-quench or sol-gel techniques.^{14–22} Hence, the results of the current study do not challenge those discussed previously in refs 24 and 26–29 but merely *confine* the current MBG structural picture on several aspects, particularly regarding the roles of Ca and P relative to that of Si. An NMR study of the evolution of the glass network structure, as well as that of the calcium phosphate phase, is in progress for a series of SBF-exposed MBG specimens; those results will be presented elsewhere.

Acknowledgment. This work was supported by the Swedish Research Council (VR), the Carl Trygger Foundation, and CICYT Spain (project MAT2005-01486). We thank Zheng Weng for instrumental NMR support, Yasuhiro Sakamoto and Andy Y. H. Lo for discussions, and the reviewers for helpful comments.

Supporting Information Available: Additional discussion of the assignment of the ^{31}P NMR spectra and double-quantum ^{31}P and ^1H results; ^1H NMR spectra of heat-treated samples as well as from spin-echo measurements (including discussion thereof); textural properties and TEM images of the MBG specimens. This material is available free of charge via the Internet at <http://pubs.acs.org>.

References and Notes

- Hench, L. L.; Splinter, R. J.; Allen, W. C.; Greenlee, T. K. *J. Biomed. Mater. Res.* **1971**, *2*, 117.
- Hench, L. L. *J. Am. Ceram. Soc.* **1991**, *74*, 1487.
- Vallet-Regí, M.; Ragel, C. V.; Salinas, A. J. *Eur. J. Inorg. Chem.* **2003**, 1029.
- Grynpas, M. D.; Omelon, S. *Bone* **2007**, *41*, 162.
- Jokinen, M.; Rahiala, H.; Rosenholm, J. B.; Peltola, T.; Kangasniemi, I. *J. Sol-Gel Sci. Technol.* **1998**, *12*, 159.
- Li, R.; Clark, A. E.; Hench, L. L. *J. Appl. Biomater.* **1991**, *2*, 231.
- Peltola, T.; Jokinen, M.; Rahiala, H.; Levänen, E.; Rosenholm, J. B.; Kangasniemi, I.; Yli-Urpo, A. *J. Biomed. Mater. Res.* **1999**, *44*, 12.
- Izquierdo-Barba, I.; Salinas, A. J.; Vallet-Regí, M. *J. Biomed. Mater. Res.* **1999**, *47*, 243.
- Martínez, A.; Izquierdo-Barba, I.; Vallet-Regí, M. *Chem. Mater.* **2000**, *12*, 3080.
- Salinas, A. J.; Martín, A. I.; Vallet-Regí, M. *J. Biomed. Mater. Res.* **2002**, *61*, 524.
- Yan, H. W.; Zhang, K.; Blanford, C. F.; Francis, L. F.; Stein, A. *Chem. Mater.* **2001**, *13*, 1374.
- Saravanapavan, P.; Jones, J. R.; Pryce, R. S.; Hench, L. L. *J. Biomed. Mater. Res.* **2003**, *66A*, 110.
- Ebisawa, Y.; Kokubo, T.; Ohura, K.; Yamamuro, T. *J. Mater. Sci.: Mater. Med.* **1990**, *1*, 239.
- Yang, W.-H.; Kirkpatrick, R. J.; Turner, G. *J. Am. Ceram. Soc.* **1986**, *69*, C222.
- Galliano, P. G.; Porto López, J. M.; Varet, E. L.; Sobrados, I.; Sanz, J. *Mater. Res. Bull.* **1994**, *29*, 1297.
- Lockyer, M. W. G.; Holland, D.; Dupree, R. *J. Non-Cryst. Solids* **1995**, *188*, 207.
- Lockyer, M. W. G.; Holland, D.; Dupree, R. *Phys. Chem. Glasses* **1995**, *36*, 22.
- Hayakawa, S.; Tsuru, K.; Iida, H.; Ohtsuki, C.; Osaka, A. *J. Ceram. Soc. Jpn., Int. Ed.* **1996**, *104*, 1003.
- Elgayar, I.; Aliev, A. E.; Boccaccini, A. R.; Hill, R. G. *J. Non-Cryst. Solids* **2005**, *351*, 173.
- Coleman, N. J.; Bellantone, M.; Nicholson, J. W.; Mendham, A. P. *Ceram. Silik.* **2007**, *51*, 1.
- Lin, K. S. K.; Tseng, Y.-H.; Mou, Y.; Hsu, Y.-C.; Yang, C.-M.; Chan, J. C. C. *Chem. Mater.* **2005**, *17*, 4493.
- Skipper, L. J.; Sowrey, F. E.; Rashid, R.; Newport, R. J.; Lin, Z.; Smith, M. E. *Phys. Chem. Glasses* **2005**, *46*, 372.
- Carta, D.; Pickup, D. M.; Knowles, J. C.; Ahmed, I.; Smith, M. E.; Newport, R. J. *J. Non-Cryst. Solids* **2007**, *353*, 1759.
- Yan, X. X.; Yu, C. Z.; Zhou, X. F.; Tang, J. W.; Zhao, D. Y. *Angew. Chem., Int. Ed.* **2004**, *43*, 5980.
- Brinker, C. J.; Lu, Y. F.; Sellinger, A.; Fan, H. *Adv. Mater.* **1999**, *11*, 579.
- Yan, X. X.; Deng, H. X.; Huang, X. H.; Lu, G. Q.; Qiao, S. Z.; Zhao, D. Y.; Yu, C. Z. *J. Non-Cryst. Solids* **2005**, *351*, 3209.
- Yan, X. X.; Huang, X. H.; Yu, C. Z.; Deng, H. X.; Wang, Y.; Zhang, Z. D.; Qiao, S. Z.; Lu, G.; Zhao, D. Y. *Biomaterials* **2006**, *27*, 3396.
- López-Noriega, A.; Arcos, D.; Izquierdo-Barba, I.; Sakamoto, Y.; Terasaki, O.; Vallet-Regí, M. *Chem. Mater.* **2006**, *18*, 3137.
- Shi, Q. H.; Wang, J. F.; Zhang, J. P.; Fan, J.; Stucky, G. D. *Adv. Mater.* **2006**, *18*, 1038.
- Xia, W.; Chang, J. J. *Controlled Release* **2006**, *110*, 522.
- Li, X.; Wang, X. P.; Chen, H. R.; Jiang, P.; Dong, X. P.; Shi, J. L. *Chem. Mater.* **2007**, *19*, 4322.
- Yun, H. S.; Kim, S.; Hyeon, Y.-T. *Chem. Commun.* **2007**, 2139.
- Kaneda, M.; Tsubakiyama, T.; Carlsson, A.; Sakamoto, Y.; Ohsuna, T.; Terasaki, O.; Joo, S. H.; Ryoo, R. *J. Phys. Chem. B* **2002**, *106*, 1256.
- Beck, J. S.; Vartuli, J. C.; Roth, W. J.; Leonowicz, M. E.; Kresge, C. T.; Schmitt, K. D.; Chu, C. T. W.; Olson, D. H.; Sheppard, E. W.; McCullen, S. B.; Higgins, J. B.; Schlenker, J. L. *J. Am. Chem. Soc.* **1992**, *114*, 10834.
- Zhao, D. Y.; Huo, Q. S.; Feng, J. L.; Chmelka, B. F.; Stucky, G. D. *J. Am. Chem. Soc.* **1998**, *120*, 6024.
- Metz, G.; Wu, X. L.; Smith, S. O. *J. Magn. Reson. A* **1994**, *110*, 219.
- Ernst, R. R.; Bodenhausen, G.; Wokaun, A. *Principles of Nuclear Magnetic Resonance in One and Two Dimensions*; Clarendon Press: Oxford, 1987.
- Rothwell, W. P.; Waugh, J. S.; Yesinowski, J. P. *J. Am. Chem. Soc.* **1980**, *102*, 2637.
- Aue, W. P.; Roufosse, A. H.; Glimcher, M. J.; Griffin, R. G. *Biochemistry* **1984**, *23*, 6110.
- Jäger, C.; Welzel, T.; Meyer-Zaika, W.; Eppe, M. *Magn. Reson. Chem.* **2006**, *44*, 573.
- MacKenzie, K. J. D.; Smith, M. E. *Multinuclear Solid-State NMR of Inorganic Materials*; Pergamon Press: Amsterdam, 2002.
- Edén, M.; Levitt, M. H. *J. Magn. Reson.* **1998**, *132*, 220.
- Yesinowski, J. P.; Eckert, H. *J. Am. Chem. Soc.* **1987**, *109*, 6274.
- Lesage, A.; Bardet, M.; Emsley, L. *J. Am. Chem. Soc.* **1999**, *121*, 10987.
- Marin-Montesinos, I.; Brouwer, D. H.; Antonioli, G.; Lai, W. C.; Brinkmann, A.; Levitt, M. H. *J. Magn. Reson.* **2005**, *177*, 330.
- Engelhardt, G.; Michel, D. *High-Resolution Solid-State NMR of Silicates and Zeolites*; Wiley: Chichester, 1987.
- Chuang, I. S.; Kinney, D. R.; Maciel, G. E. *J. Am. Chem. Soc.* **1993**, *115*, 8695.
- Christiansen, S. C.; Zhao, D. Y.; Janicke, M. T.; Landry, C. C.; Stucky, G. D.; Chmelka, B. F. *J. Am. Chem. Soc.* **2001**, *123*, 4519.
- Liu, C. C.; Maciel, G. E. *J. Am. Chem. Soc.* **1996**, *118*, 5103.
- Baccile, N.; Laurent, G.; Bonhomme, C.; Innocenzi, P.; Babonneau, F. *Chem. Mater.* **2007**, *19*, 1343.
- Melosh, N. A.; Lipic, P.; Bates, F. S.; Wudl, F.; Stucky, G. D.; Fredrickson, G. H.; Chmelka, B. F. *Macromolecules* **1999**, *32*, 4332.
- Engelhardt, G.; Nofz, M.; Forkel, K.; Wihsmann, F. G.; Mägi, M.; Samoson, A.; Lippmaa, E. *Phys. Chem. Glasses* **1985**, *26*, 157.
- Zhang, P.; Grandinetti, P. J.; Stebbins, J. F. *J. Phys. Chem. B* **1997**, *101*, 4004.
- Maciel, G. E.; Sindorf, D. W. *J. Am. Chem. Soc.* **1980**, *102*, 7606.
- Eckert, H.; Yesinowski, J. P.; Silver, L. A.; Stolper, E. M. *J. Phys. Chem.* **1985**, *92*, 2055.
- Zhuravlev, L. T. *Colloids Surf., A* **2000**, *173*, 1.
- Grünberg, B.; Emmeler, T.; Gedat, E.; Shenderovich, I.; Findenegg, G. H.; Limbach, H. H.; Buntkowsky, G. *Chem.—Eur. J.* **2004**, *10*, 5689.
- Trébosc, J.; Wiench, J. W.; Huh, S.; Lin, V. S.-Y.; Pruski, M. *J. Am. Chem. Soc.* **2005**, *127*, 3057.
- Alam, T. M.; Fan, H. Y. *Macromol. Chem. Phys.* **2003**, *204*, 2023.
- Hu, J. Z.; Kwak, J. H.; Herrera, J. E.; Wang, Y.; Peden, C. H. F. *Solid State Nucl. Magn. Reson.* **2005**, *27*, 200.
- Bae, Y. K.; Han, O. H. *Microporous Mesoporous Mater.* **2007**, *106*, 304.
- Hartmeyer, G.; Marichal, C.; Lebeau, B.; Rigolet, S.; Caulet, P.; Hernandez, J. *J. Phys. Chem. C* **2007**, *111*, 9066.
- Nivaggioli, T.; Tsao, B.; Alexandridis, P.; Hatton, T. A. *Langmuir* **1995**, *11*, 119.
- Brinker, C. J.; Keefer, K. D.; Schaefer, D. W.; Assink, R. A.; Kay, B. D.; Ashley, C. S. *J. Non-Cryst. Solids* **1984**, *63*, 45.
- Hohwy, M.; Jakobsen, H. J.; Edén, M.; Levitt, M. H.; Nielsen, N. C. *J. Chem. Phys.* **1998**, *108*, 2686.
- Santos, R. A.; Wind, R. A.; Bronnimann, C. E. *J. Magn. Reson. B* **1994**, *105*, 183.